

Multifractal nature of plume structure in high Rayleigh number convection

By **BABURAJ A. PUTHENVEETTIL**, ¹
G. ANANTHAKRISHNA ²†
AND JAYWANT H. ARAKERI ¹

¹Department of Mechanical Engineering, ²Materials Research Center,
 Indian Institute of Science, Bangalore, India

(Received July 2004)

The geometrically different plan forms of near wall plume structure in turbulent natural convection, visualised by driving the convection using concentration differences across a membrane, are shown to have a common multifractal spectrum of singularities for Rayleigh numbers in the range $10^{10} - 10^{11}$ at Schmidt number of 602. This common scaling is seen to be valid for a length scale range of 2^5 and is independent of the Rayleigh number, the flux, the strength and nature of the large scale flow, and the aspect ratio. Similar scaling is observed for the plume structures obtained in the presence of a weak flow across the membrane. The universality of this non trivial spatial scaling is proposed to be due to the common underlying generating process of the near wall plume structure.

1. Introduction

Turbulent Rayleigh - Bénard convection and other related natural convection flows at high Rayleigh numbers (Ra) have many unresolved issues like the phenomenology of flux scaling, the presence of coherent large scale circulation and its effects on the near wall boundary layers, the exponential nature of the probability distribution function of temperature fluctuations and the Prandtl Number (Pr) dependence. These are extensively discussed in the reviews of Siggia (1994) and Adrian, Ferreira & Boberg (1986). It is clear from these reviews that very little is known about the nature of near wall coherent structures at high Ra . Further, as most studies are conducted in cryogenic conditions - which prevent visualisation of the near wall structures - there are no quantitative studies on the patterns of near wall coherent structures in high Ra turbulent convection. The non-dimensional parameters that characterise natural convection flows are the Rayleigh number ($\text{Ra} = g \frac{\Delta \rho}{\rho} H^3 / \nu \alpha$, the ratio of buoyancy effects to dissipative effects); Prandtl number ($\text{Pr} = \nu / \alpha$, a fluid property) and aspect ratio ($\text{AR} = L / H$, a geometric parameter of the fluid layer) where, g = the acceleration due to gravity, $\frac{\Delta \rho}{\rho}$ = nondimensional density difference, H = fluid layer height, L = fluid layer width, ν = kinematic viscosity and α = thermal diffusivity.

Most of the previous studies on near wall coherent structures in turbulent convection give only a qualitative picture at relatively low Ra of $10^6 - 10^8$ at $\text{Pr} = 6$. Closed polygonal shapes formed from line plumes are seen at lower Ra , which change to randomly moving and merging line plume patterns at higher Ra of $10^7 - 10^8$ (Spangenberg & Rowland 1961; Tamai & Asaeda 1984; Sparrow & Husar 1969; Kitamura & Kimura 1995; Theerthan & Arakeri

† garani@mrc.iisc.ernet.in

2000). Line plumes are buoyant fluid rising in the form of sheets from lines on the horizontal heated surface. Similar observations are also seen from direct numerical simulations. (Kerr & Herring 2000; Schmidt & Schumann 1989). Visualisations at the highest Ra so far ($\sim 10^9$) by Zocchi, Moses & Libchaber (1990) show line plumes being swept along the direction of shear caused by the large scale flow. Theerthan & Arakeri (1998) showed that the randomly spaced and oriented plumes near the wall can be modeled as a regular array of laminar line plumes, each plume fed by boundary layers on either side. Puthenveetttil (2004) extended the analysis to high Ra, high Pr case and found that the distribution of plume spacings have a common log-normal distribution independent of the parameter values. None of these studies address the spatial scaling of the plume structure pattern.

In this paper, we report the results of investigations on the spatial scaling of the near wall plan-form plume structures in high Rayleigh number turbulent free-convection using multifractal formalism. The initial motivation for using multifractal analysis was from the dendritic and the fractal like appearance of some of the structures. The apparent scale free nature and the non-uniformity of the structures pointed to their possible multifractal nature. Further, log-normal distributions are created by multiplicative processes, commonly analysed by the multifractal formalism. Briefly, multifractal formalism describes the statistical properties of singular measures (often resulting from any multiplicative process) in terms of the singularity spectrum $f(\alpha)$, corresponding to the singularity strength α . Then, in simple terms, $f(\alpha)$ can be regarded as the fractal dimensions of subsets with corresponding singularity strength α . The details of multifractal formalism can be seen in Meneveau & Sreenivasan (1991); Mandelbrot (1989); Feder (1988); Paladin & Vulpiani (1987), Halsey, Jenson, Kadanoff, Procaccia & Shraiman (1986), and the references cited therein. Even though studies abound on applying this formalism for characterising spatial structures in various fields, we are not aware of such an analysis of near wall coherent structures of turbulent convection.

2. Experimental setup and image preprocessing

We visualise the near wall plume structure at high Ra by driving the convection using concentration differences of NaCl across a membrane. High Ra ($10^{10} - 10^{11}$) are achieved at Schmidt number ($Sc \sim \nu/D$, equivalent to Pr) of 602 due to the low molecular diffusivity (D) of NaCl. The set-up consists of two glass compartments of square cross section, arranged one on top of the other with a fine membrane fixed horizontally in between them. A schematic of the experimental set up is shown in Figure 2. The membranes used are Pall GelmannTM NX29325 membrane disc filters (PG henceforth) with a random pore structure having a mean pore size of 0.45μ and Swedish Nylobolt 140S screen printing membrane (140s henceforth) with a regular square pore of size $35\mu \times 35\mu$. The bottom tank was filled with distilled water tagged with a small amount of Sodium Fluoresceine (absorption spectra peak at 488nm and emission spectra peak at 518nm) and then the top tank filled with brine to initiate the experiment. The convection is unsteady, but quasi-steady approximation can be used. A horizontal laser sheet, expanded and collimated from a 5W Spectra Physics StabiliteTM 2017 Ar- Ion laser at 488nm is passed just above (<1 mm) the membrane. The dye in the bottom solution while convecting upward fluoresces on incidence of the laser beam to make the plume structure visible. A schematic of the visualisation of the near wall phenomena is shown in Figure 2(b) and (c). A visible long pass filter glass, Coherent optics OG-515, is used to block any scattered laser light and allow the emitted fluorescence to pass through. The images are captured on a digital handycam Sony DCR PC9E. Experiments are conducted in 23 cm high tanks, with one tank having $15\text{ cm} \times 15\text{ cm}$ ($AR = 0.65$) cross section and another

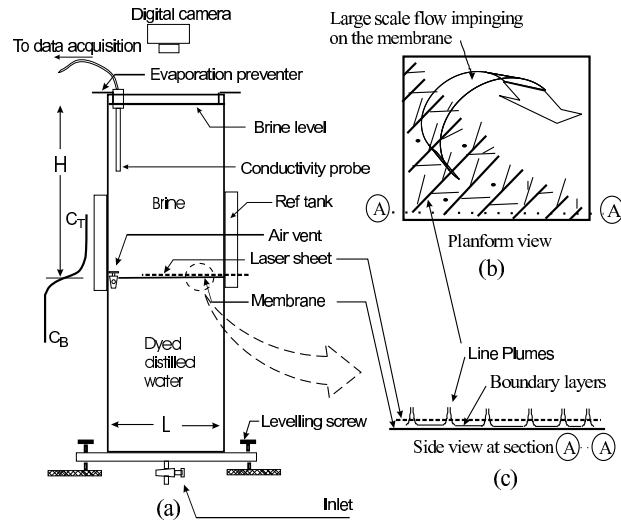


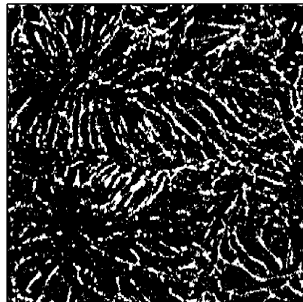
FIGURE 1. Experimental set up and the visualisation process. (a) The overall set up (b) The plan form view of the near wall plume structure as seen at the intersection of a horizontal laser sheet. (c) The side view in a vertical plane showing rising line plumes. The planform in (b) is for the TF-type convection showing a plume free area where the large scale flow impinges on the membrane.

with $10\text{ cm} \times 10\text{ cm}$ ($AR = 0.435$) cross section. Starting top tank concentrations of 10 g/l , 7 g/l and 3 g/l were used to study the plume structure under different Ra . Further details of the experimental set-up and the procedure are given in Puthenveettil (2004).

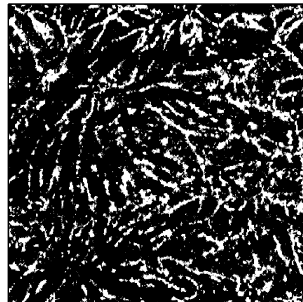
The Laser Induced Fluorescence (LIF) images captured by the camera were RGB 24bit color with 640×480 pixels resolution. The multifractal analysis is conducted on binary images obtained from these RGB images. In using binary images, we are essentially neglecting the intensity variation of the fluorescence (proportional to the concentration of the dye) within the plume line thickness. The analysis is hence valid only for the geometrical aspects of the planform. The RGB image was cropped to remove the tank walls, converted to gray scale, Radon transformed to remove the lines in the image (formed due to imperfections in the optics and test section surface) and then re-sampled to increase the resolution. The non-uniform background illumination due to the attenuation of the laser sheet was subtracted to obtain the plume lines over a uniform dark background. Contrast and intensity were enhanced to make the plume lines clearer before converting to a black and white binary image using a threshold. The effect of thresholding on the multifractal exponents is considered in Appendix A. The binary image is seen to retain almost all the features of the raw image.

3. The plume structure planforms

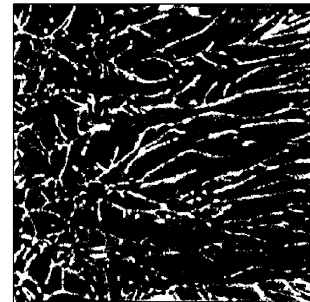
Figure 2 shows the binary images of the various planform plume structures obtained in the experiments. The parameter values are shown below each image. $\Delta C(\text{g/l})$ is the effective driving concentration difference on the side of the membrane where the structure is visualised, Ra is based on this ΔC and H (top tank fluid layer height), Q denotes the flux of NaCl in $\text{mg/cm}^2/\text{min}$ and $W_* \sim (g\beta Q H)^{1/3}$ (Deardorff 1970) is an estimate of the large scale flow strength, where β is the coefficient of salinity. The white lines in the figures are the bases of the sheet plumes originating from the membrane surface. Two types of convection are observed depending on the pore size of the membrane. In one



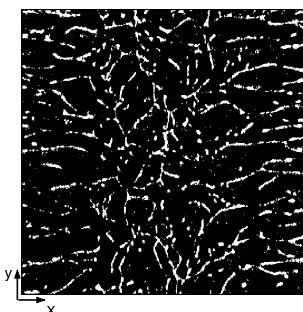
(a) PG membrane in 15 cm \times 15 cm tank, Ra = 2.04×10^{11} , ΔC = 3.2 g/l, Q = 0.1 mg/cm 2 /min, W_* = 0.31 cm/s, Image area=14.65 cm square, 714 2 pix



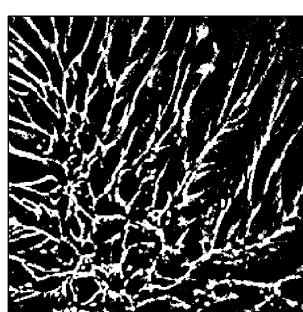
(b) Structure after 30seconds from (a) Ra = 2.03×10^{11} , ΔC = 3.19 g/l, Q = 0.1 mg/cm 2 /min, W_* = 0.31 cm/s, Image area=13.74 cm square, 728 2 pix



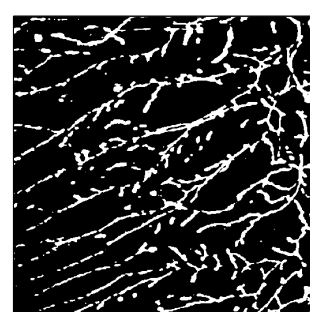
(c) PG membrane in 10 cm \times 10 cm tank, Ra = 2.03×10^{11} , ΔC = 3.198 g/l, Q = 0.11 mg/cm 2 /min, W_* = 0.31 cm/s, Image area= 9.157 cm square, 728 2 pix



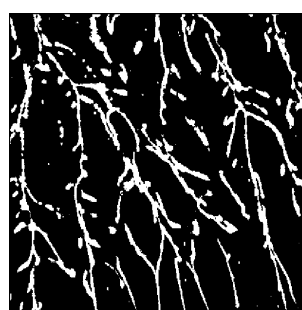
(d) PG membrane in 15 cm \times 15 cm tank, Ra = 5.56×10^{10} , ΔC = 0.875 g/l, Q = 0.02 mg/cm 2 /min, W_* = 0.18 cm/s, Image area=12.83 cm square, 728 2 pix



(e) 140s membrane in 15 cm \times 15 cm tank, Ra = 5×10^{11} , ΔC = 7.87 g/l, Q = 0.39 mg/cm 2 /min, W_* = 0.47 cm/s, V_I = 0.002 cm/s, Image area= 8.61 cm square, 528 2 pix



(f) 140s membrane in 15 cm \times 15 cm tank, Ra = 4.49×10^{11} , ΔC = 7.06 g/l, Q = 0.41 mg/cm 2 /min, W_* = 0.48 cm/s, V_I = 0.0023 cm/s, Image area= 8.32 cm square, 520 2 pix



(g) 140s membrane in 15 cm \times 15 cm tank, Ra = 5.36×10^{11} , ΔC = 8.42 g/l, Q = 0.41 mg/cm 2 /min, W_* = 0.48 cm/s, V_I = 0.0016 cm/s, Image area= 7.58 cm square, 616 2 pix

(h) 140s membrane in 15 cm \times 15 cm tank, Ra = 1.65×10^{11} , ΔC = 2.6 g/l, Q = 0.07 mg/cm 2 /min, W_* = 0.27 cm/s, Image area= 14.69 cm square, 714 2 pix

case, the transport of salt through the membrane is by diffusion. In the second case, the transport is due to a flow, albeit weak, across the membrane. In both cases, the line plumes emanate from the thin unstable boundary layers above the membrane. As the focus of this paper is on the spatial scaling of these structures, we only give a brief description of the phenomena in each image of Figure 2; the details are discussed in Puthenveettil (2004).

3.1. Planforms in D-Type convection

For the lower pore sized (PG 0.45μ) membrane, the transport across the partition would become diffusion dominated (D-type henceforth), while the transport above and below the membrane becomes similar to Rayleigh - Bénard convection at high Ra. Figures 2(a) to 2(d) show the structures obtained in the D-type convection. The first two images are from the larger $AR = 0.65$ which had multiple large scale flow cells, the signatures of which are seen as circular patches with aligned line plumes oriented radially around the patches, the plume free circular patch being the area where the large scale circulation impinges on the membrane. Figure 2(c) shows the planform of plume structure under the same conditions as in Figures 2(a) and 2(b), but in the smaller ($10\text{ cm} \times 10\text{ cm}$, $AR=0.435$) cross sectional area tank. In this case, there was only a single large scale circulation which was rotating clockwise in the x-z plane and aligning the near wall plumes in the x-direction (See Figure 2(d) for the co-ordinate directions, z is normal to the figure). The plume structure at lower Ra in the larger $AR = 0.65$ tank is seen in Figure 2(d). There were two counter rotating circulation cells (anticlockwise on the left and clockwise on the right) rotating in the x-z plane which created a near wall mean shear directed toward the center along the x direction. In all these images the flux scaled approximately as $\Delta C^{4/3}$, as in turbulent Rayleigh - Bénard convection.

3.2. Planforms in TF-Type convection

Experiments with the coarser ($140s, 35\mu$) membrane showed that only half the area above the membrane was covered by plumes, with the other half having plumes below the membrane. This structure is due to a weak through flow across the membrane (TF type henceforth). The lower fluid dynamic resistance of the coarser membrane allows this through flow. The region having plumes on top of the membrane corresponds to upward through flow and vice versa (See schematic in Figure 2(b)). The through flow velocities V_I are about 10 times smaller than the near wall velocity scales in turbulent free convection given by $W_o \sim (g\beta QD)^{1/4}$ (Townsend 1959). Figure 2(e) to 2(g) show the plan form view of the plume occupied region in the TF type convection at $AR = 0.65$. Figure 2(e) shows the corner region of this structure when there was a near wall mean shear toward the bottom left corner due to a diagonally oriented large scale circulation rotating in the clockwise direction. Figure 2(f) shows a similar corner view of the structure when there is a near wall mean shear along the diagonal toward the top right corner, created by an anticlockwise circulation. The central zoomed view, where the mean shear effects are predominant, in a structure similar to that in Figures 2(e) and 2(f) is shown in Figure 2(g). In all these cases, the flux scaled as ΔC^3 due to the presence of a flow across the membrane. The phenomenology behind this flux scaling is described in Puthenveettil (2004). The TF-type convection in the $140s$ membrane experiments was seen to change to the D-type with $Q \sim \Delta C^{4/3}$ scaling at lower driving potentials. Figure 2(h) shows one type of plume structure obtained in such a situation.

In both the D-type and the TF-type convection, the plume structure is formed due to the boundary layers becoming unstable at different spatial locations giving rise to line plumes, which then merge together due to the entrainment effect of the nearby plumes.

The mean shear due to the large scale circulation generally aligns the plume lines in the direction of the shear. New plumes are generated at the vacant spaces created by this merger. Even though the geometrical structures of the plumes are continuously evolving spatio-temporal patterns, for a given set of parameters they appear to exhibit a statistical stationary state. The generating process seems to have some common characteristics reflected in the common log-normal probability distribution function of the spacings found by Puthenveettil (2004). Log-normal processes are usually the outcome of multiplicative process. As the multifractal approach is a natural tool for the analysis of multiplicative processes, we analyse the plume structure using multifractal analysis.

4. Multifractal analysis

4.1. Methodology and Scaling range

We use the standard box counting methodology (Feder 1988) to estimate the multifractal exponents. The analysis is done on square binary images (L^2 pixels). For each moment q , the partition function $Z_q = \sum_{i,j} P_{i,j}^q$ is calculated for various box sizes (l_b in pixels) and the slope of $\ln Z_q$ Vs $\ln \frac{l_b}{L}$ gives the Cumulant generating function $\tau(q)$ defined through $\sum_{i,j} P_{i,j}^q \sim (l_b/L)^{\tau(q)}$ where, the measure $P_{i,j}$ is the probability of occurrence of the plume in a box (ratio of white pixels in each box to the total number of white pixels in the image) and i, j are the box indices. $\tau(q) = (q-1)D_q$ with D_q referring to q -th order Renyi dimension. The number of boxes where $P_{i,j} \sim l_b^\alpha$ has a singularity strength between α and $\alpha + d\alpha$ is given by $N(\alpha) \sim l_b^{-f(\alpha)}$. $f(\alpha)$ is the fractal dimension of the subset - picked out by each value of the moment q - with singularity strength α . The Hölder exponent α and $f(\alpha)$ are calculated using the direct method due to Chabra & Jenson (1989). The expressions for $f(\alpha)$ and α are

$$f(\alpha) = \lim_{l_b \rightarrow 0} \frac{\sum_{i,j} \mu_{i,j} \ln \mu_{i,j}}{\ln(l_b/L)}, \quad \alpha(q) = \lim_{l_b \rightarrow 0} \frac{\sum_{i,j} \mu_{i,j} \ln P_{i,j}}{\ln(l_b/L)}, \quad (4.1)$$

where $\mu_{i,j} = \frac{P_{i,j}^q}{\sum_{i,j} P_{i,j}^q}$ are the normalized measures. For each value of the moment q , the slope of the log-log plots of the relevant quantities in Equations. (4.1) in the range of values where the plots are linear, give $f(q)$ and $\alpha(q)$. In our work, the range of q values is limited to $-2 \leq q \leq 5$ in order to have a reasonable range of scaling regime.

The estimation of $f(\alpha)$ and α for the image in Figure 2(e) is shown in Figure 3. The image size was 8.61 cm square sampled at 528^2 pixels ($L = 528$). The calculation was done for box sizes $l_b = 528, 264, 176, 132, 88, 66, 48, 44, 33, 24$ and 22 pixels. Figure 3(a) shows the plots of $\sum_{i,j} \mu_{i,j} \ln \mu_{i,j}$ versus $\ln(l_b/L)$ for a few typical values of $q = -2, 0.5$ and 5. The slope of the linear fit in the range $66 \text{ pix} \leq l_b \leq 528 \text{ pix}$, (i.e., from 1.076 to 8.61 cm) was used to estimate $f(\alpha(q))$ for all q . This slope is valid for a larger length scale range of $22 \text{ pix} \leq l_b \leq 528 \text{ pix}$, (i.e. from 0.359 to 8.61 cm) for $q = -0.5$ and 5.0, while for $q = -2$, the linearity holds only in the fit range. The ranges for various q values are the same for estimating $\alpha(q)$ and τ from the plots of $\sum_{i,j} \mu_{i,j} \ln P_{i,j}$ vs $\ln(l_b/L)$ (Figure 3(b)) and $\ln \sum_{i,j} P_{i,j}^q$ vs $\ln(l_b/L)$ (Figure 3(c)) respectively. Figure 3(a) to 3(c) show that the deviation from the linearity is pronounced for $q = -2$ below a specific box size of around 1cm ($\ln(l_b/L) = -2$), while it is almost negligible for positive moments. This behavior is also seen in other studies like Chabra, Meneveau, Jenson & Sreenivasan (1989) and Meneveau & Sreenivasan (1991). As negative moments amplify low measures, and the effect of noise in the low measure regions at smaller box sizes is substantial, we expect this deviation to be due to the amplification of the errors. For the same reason,

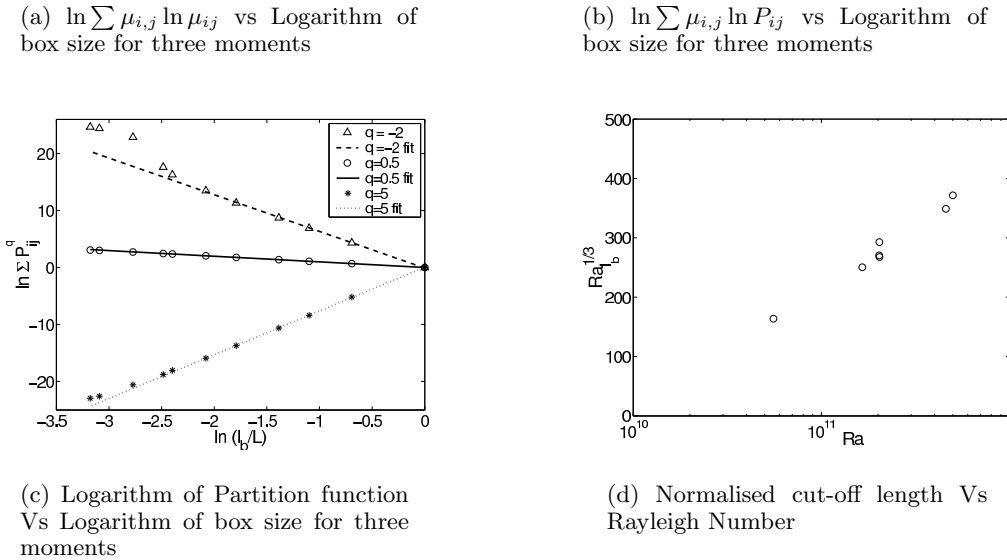


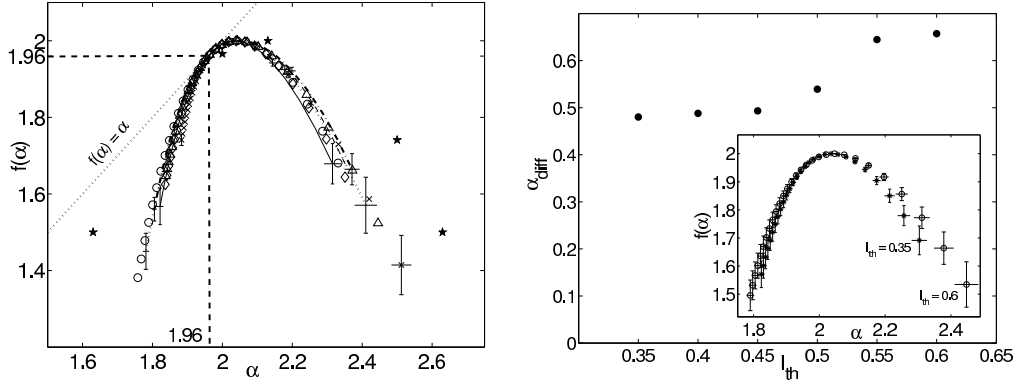
FIGURE 3. The range of multifractal scaling for moments $q = -2, 0.5$ and 5 . Figure 3(a), 3(b) and 3(c) show the scaling range for $f(\alpha)$, α and τ respectively. The lines show the linear fit used for calculating the slopes. Figure 3(d) shows the dependence of normalised cut-off length on Rayleigh Number

the negative moment slopes were also the most affected when the binary image threshold was changed (See inset of Figure 4(b)).

The analysis was carried out for all the images in Figure 2. The major common observations from the plots of $\sum_{i,j} \mu_{i,j} \ln \mu_{i,j}$ and $\sum_{i,j} \mu_{i,j} \ln P_{i,j}$ vs $\ln(l_b/L)$ for these images can be summarized as follows.

(a) For moments $q \geq -1$, the linearity of the above quantities is seen to hold till about 0.5 cm. As positive moments pick out areas of higher measure, these moments represent the main plume structure. Thus, the main plume structure shows a multifractal scaling in the range of tank cross section to 0.5 cm i.e., a range of 2^5 .

(b) When negative moments are less than -1, the plots of these quantities show a deviation from linearity at about 1 cm in all the images. Figure 3(d) shows this cut-off length for all the images, normalised by the near wall length scale in turbulent free convection $Z_w = \left(\nu D / g \frac{\Delta \rho}{\rho} \right)^{1/3}$ (Theerthan & Arakeri 1998), as a function of Ra . $l_b/Z_w = Ra_{l_b}^{1/3}$, where Ra_{l_b} is the Rayleigh number based on this cutoff length and the effective concen-



(a) The multifractal spectrum, f Vs α for all the images analysed. Figure 2(a), - - - Figure 2(b), \circ Figure 2(c), — Figure 2(d), \times Figure 2(e), \diamond Figure 2(f), \triangle Figure 2(g), - - - Figure 2(h), \star Meneveau & Sreenivasan (1991)

(b) Variation of $\alpha_{diff} = \alpha_{max} - \alpha_{min}$ with the threshold I_{th} for Figure 2(d). The inset shows the $f - \alpha$ curve for the two extreme thresholds

FIGURE 4. the multifractal spectrum and the sensitivity to image quality

tration difference on one side of the membrane. It is seen that the normalized cut-off lengths increase almost linearly with Ra . Hence, for negative moments $q < -1$, the multifractal scaling is valid for a shorter length scale range of tank cross section to 1 cm, i.e. $\sim 2^4$.

(c) There seems to be a further lower cut off of approximately 5 mm, below which the slope of $\sum_{i,j} \mu_{i,j} \ln P_{i,j}$ Vs l_b/L for $q \leq 1$ goes to zero (See Figure 3(b) at $\ln(l_b/L) \sim -2.75$). This is expected to be because the smallest length scales in the image, viz. the plume line thicknesses, are of the same order.

4.2. The multifractal spectrum

The $f - \alpha$ curves of all the images in Figure 2 are shown in Figure 4(a). The error bars in the figure are the errors in the slope of the linear curve fits. The value of f at $q = 0$ is the fractal dimension of the ‘support’ of the measure. As the underlying area over which the plumes are formed is a non-fractal surface, $f(\alpha(0)) = 2$. Figure 4(a) shows that this is satisfied, suggesting a good level of confidence in the calculation. We also note that the fractal dimension corresponding to the (information) entropy $S = \sum_{\beta=0}^{b-1} p_{\beta} \log_b p_{\beta}$, of the underlying process which generates these structures is 1.96.

The results of our analysis of the near wall plume structure in turbulent free-convection at high Ra are strongly suggestive of its multifractal nature. Even though the Ra based on the concentration difference on one side of the membrane varies only about a decade, the analyzed images cover a wide range of conditions. The images show a wide variety of structures with single and multiple large scale flow cells, aligned and random structures, different test section cross sectional areas ($10 \times 10 \text{ cm}^2$ and $15 \times 15 \text{ cm}^2$), absence and presence of a flow through the membrane, different large scale flow strengths (about 2.5 times) and a wide range of flux (over two decades). The plot of Figure 4(a) show that, within the errors encountered in the current analysis, all these images have the same multifractal scaling of the main plume structure for length scales greater than 0.5 cm.

5. Discussion and Conclusions

We have seen that the plan forms of near wall plume structure in high Ra turbulent free-convection under varying parameter values have the same multifractal spectrum of singularities. Hence, the plan forms that appear substantially different in their geometric form have the same non trivial spatial scaling. The probabilistic interpretation of multifractal formalism, as described by Mandelbrot (1989), shows that f and α indirectly describe the underlying generating mechanism of these structures in terms of the multipliers for each stage of the process. Thus, a common $f(\alpha)$ curve over different length scales for these plume structures implies the existence of a common distribution of multipliers. The repeated composition of this multiplier distribution is the underlying cause of the scaling properties. In physical terms, this means that the present images have the same underlying generating mechanism. The common generating mechanism that can be identified here is that the thin layer of lighter fluid above the membrane becomes unstable resulting in the generation of sheet plumes. Interaction of the neighboring plumes due to entrainment leads to their merger, new plumes are nucleated in the vacant space due to the merger, the whole process being influenced by the external flow field created by the mean wind.

In earlier studies, it was shown that the spacings between the plume lines have a universal standard log-normal form (Puthenveetttil 2004). Log-normal distributions arise when the underlying process is a multiplicative process. Specifically, log-normal distributions can be shown to correspond to a quadratic approximation of $f(\alpha)$ around its support dimension valid only in the neighborhood of small q values (Meneveau & Sreenivasan 1991; Paladin & Vulpiani 1987). For multinomial processes, f is calculated as the maximum from a range of values for any α for each moment q . Connecting this with the thermodynamic analogy noted in the literature (Feder 1988; Chabra, Meneveau, Jenson & Sreenivasan 1989), the common $f - \alpha$ curves might imply that the plume structure in turbulent convection is formed so as to maximize the entropy of the structure.

Earlier studies on the multifractal nature of energy dissipation field in turbulent flows by Meneveau & Sreenivasan (1991) have parallels with the current study. The energy dissipation is caused by the velocity gradients at the viscous scales. Plume edges represent the major gradients of velocities near the wall in convection. These also are the relevant viscous scales near the wall. Hence, it is possible that the near wall energy dissipation field follows the plume structure closely. The $f - \alpha$ curves obtained by Meneveau & Sreenivasan (1991) are shown in comparison with the present curves in Figure 4(a). The $f(\alpha)$ curves obtained in our case have a lower spread. Further work is needed to clarify the possible connection of these energy dissipation studies to the present analysis.

Appendix A. Effect of thresholding

The correctness of the calculated multifractal exponents depends on how well the essential plume structure features in the raw image are retained by the binary image. If the binary threshold ($0 \leq I_{th} \leq 1$) is larger than an optimum value, the finer details of the plume structure in the raw image are cut off, while with a lower threshold, the image becomes too noisy and the plume lines become thicker than actual. Figure 4(b) shows the variation of $\alpha_{diff} = \alpha_{max} - \alpha_{min}$ with the threshold for the image in Figure 2(d). The inset in Figure 4(b) shows the $f - \alpha$ curves at the two extreme thresholds. Thresholds equal to and above 0.55 produced binary images that were clearly missing in details on visual examination. Thresholds below 0.45 created images that had a noticeably larger

plume thickness than in the raw image. Therefore, for this image, the threshold was chosen to be 0.45. The variation of α_{diff} between these two extremes was about 0.15, which was of the same order as the error in α , as estimated from the errors in slope calculation. This could be noticed in the inset in Figure 4(b), where the shift in the curve is less than the error bar size. This means that the change in the α values due to error from the optimum threshold is going to be within the error limit involved in the calculation of α . Further, the inset of Figure 4(b) shows that the threshold does not affect the form of the $f - \alpha$ curve. Hence in all the images, the threshold was chosen based on a combination of visual judgement and sensitivity analysis. The above analysis was for one of the low quality images and hence represent the worst case dependence on the threshold. For better quality images as in Figure 2(f), there was negligible variation with threshold.

REFERENCES

- ADRIAN, R., FERREIRA, R. & BOBERG, T. 1986 Turbulent thermal convection in wide horizontal fluid layers. *Experiments in Fluids* **4**, 121–141.
- CHABRA, A., MENEVEAU, C., JENSON, R. & SREENIVASAN, K. R. 1989 Direct determination of the $f(\alpha)$ singularity spectrum and its application to fully developed turbulence. *Physical Review A* **40** (9), 5284–5294.
- CHABRA, A. B. & JENSON, R. V. 1989 Direct determination of $f(\alpha)$ singularity spectrum. *Physical Review Letters* **62** (12), 1327–1330.
- DEARDORFF, J. 1970 Convective velocity and temperature scales for the unstable planetary boundary layer and for Rayleigh convection. *Journal of the Atmospheric Sciences* **27**, 1211–1213.
- FEDER, J. 1988 *Fractals*. Plenum press.
- HALSEY, T., JENSON, M., KADANOFF, L., PROCACCIA, I. & SHRAIMAN, B. 1986 Fractal measures and their singularities: the characterisation of strange sets. *Physical Review A* **33** (2), 1141–1151.
- KERR, R. M. & HERRING, J. R. 2000 Prandtl number dependence of nusselt number in direct numerical simulations. *Jl. Fluid. Mech.* **419**, 325–344.
- KITAMURA, K. & KIMURA, F. 1995 Heat transfer and fluid flow of natural convection adjacent to upward facing plates. *Int. Jl. Heat Mass Transfer* **38**, 3149–3159.
- MANDELBROT, B. B. 1989 Multifractal measures, especially for the geophysicist. *Pure and applied geophysics* **131** (1/2), 5–42.
- MENEVEAU, C. & SREENIVASAN, K. R. 1991 The multifractal nature of turbulent energy dissipation. *Jl. Fluid. Mech.* **224**, 429–484.
- PALADIN, G. & VULPIANI, A. 1987 Anomalous scaling laws in multifractal objects. *Physics Reports* **156** (4), 147–225.
- PUTHENVEETTIL, B. A. 2004 Investigations on high Rayleigh number turbulent free-convection. PhD thesis, Indian Institute of Science, Bangalore, <http://www.mecheng.iisc.ernet.in/~apbabu/thesis.pdf>.
- SCHMIDT, H. & SCHUMANN, U. 1989 Coherent structure of the convective boundary layer derived from large -eddy simulations. *Jl. Fluid. Mech.* **200**, 541–562.
- SIGGIA, E. D. 1994 High Rayleigh number convection. In *Ann Rev Fluid Mechanics*, , vol. 26, pp. 137–168.
- SPANGENBERG, W. G. & ROWLAND, W. G. 1961 Convective circulation in water induced by evaporative cooling. *Phys. Fluids* **4** (6), 743–750.
- SPARROW, E. & HUSAR, R. 1969 Longitudinal vortices in natural convection flow on inclined plates. *Jl. Fluid. Mech.* **37**, 251–255.
- TAMAI, N. & ASAEDA, T. 1984 Sheet like plumes near a heated bottom plate at large Rayleigh number. *Jl. Geophys. Res.* **89**, 727–734.
- THEERTHAN, S. A. & ARAKERI, J. H. 1998 A model for near wall dynamics in turbulent Rayleigh - Bénard convection. *Jl. Fluid. Mech.* **373**, 221–254.

- THEERTHAN, S. A. & ARAKERI, J. H. 2000 Plan form structure and heat transfer in turbulent free convection over horizontal surfaces. *Phys. Fluids* **12**, 884–894.
- TOWNSEND, A. 1959 Temperature fluctuations over a heated horizontal surface. *Jl. Fluid. Mech.* **5**, 209–211.
- ZOCCHI, G., MOSES, E. & LIBCHABER, A. 1990 Coherent structures in turbulent convection, an experimental study. *Physica A* **166**, 387–407.

